RSC Advances

PAPER

View Article Online
View Journal | View Issue

Cite this: *RSC Adv.*, 2015, **5**, 1301

Graphene/carbon aerogels derived from graphene crosslinked polyimide as electrode materials for supercapacitors

Youfang Zhang, Wei Fan, Yunpeng Huang, Chao Zhang and Tianxi Liu*

Carbon aerogels with hierarchical porous structures are highly promising for developing novel electrode materials for supercapacitors due to their substantial active sites for ion and electron transfer. Herein, a new type of graphene/carbon aerogels with multimodal pores have been facilely synthesized *via* carbonization of graphene crosslinked polyimide aerogels. Compared to most carbon aerogels based on organic aerogels reported previously, this preparation process is facilitated by the exclusion of harmful formaldehyde. Moreover, graphene is demonstrated as a powerful crosslinking agent, allowing acceleration of the gelation process, improvement of the porous structures inside carbon aerogels, and enlargement of specific surface area and conductivity of carbon aerogels. SEM observation shows the multimodal pores and three-dimensional nano-network of carbon aerogels, which provide short diffusion lengths for both charge and ion transport and high electroactive regions. With graphene involved, the as-prepared carbon aerogels possess high specific surface area up to 998.7 $m^2\ g^{-1}$ and specific capacitance up to 178.1 F g^{-1} at a current density of 1 A g^{-1}, which is much higher than that of pure carbon aerogels (193.6 $m^2\ g^{-1}$ and 104.2 F g^{-1}). This work provides a new and facile avenue for fabricating high performance carbon aerogels with hierarchical structures and broadens the potential applications of polyimide.

Received 23rd October 2014
Accepted 26th November 2014

DOI: 10.1039/c4ra13015d

www.rsc.org/advances

Introduction

Carbon aerogels have received considerable attention in recent years and have found wide applications in catalyst supports,[1] adsorption for pure water or separation of poisonous gas,[2–6] hydrogen storage and electrodes for supercapacitors, batteries and fuel cells[7–12] due to their highly continuous porosity, low density, high surface area, excellent electrical conductivity and fast mass and electron transport kinetics. Liu *et al.*[13] synthesized carbon xerogels based on polycondensation of phenol and formaldehyde crosslinked by graphene oxide (GO). The highest specific surface area, mesoporous volume, and specific capacity of their carbon xerogels were 378 $m^2\ g^{-1}$, 0.56 $cm^3\ g^{-1}$ and 116 F g^{-1}, respectively. Shen *et al.*[9] reported that the performance of resorcinol–formaldehyde based carbon aerogels can be significantly enhanced by a simple treatment with CO_2 activation. The specific surface area and the specific capacitance of the CO_2 activated carbon aerogels can be up to 3431 $m^2\ g^{-1}$ and 152 F g^{-1} at a current density of 0.3 A g^{-1} in 1 M Et_4NBF_4-AN electrolyte. Carlos Moreno-Castilla *et al.*[14] reported that Cu and Ag doped carbon aerogels obtained from resorcinol and formaldehyde and the metal-doped carbon aerogels were activated with oxygen at 300 °C. The results showed that the activated Cu-doped carbon aerogel showed the highest gravimetric and volumetric capacitances, 192 F g^{-1} and 98 F cm^{-3}, respectively. However, most of these carbon aerogels are based on resorcinol (R)–formaldehyde (F) which highly relies on the utilization of formaldehyde.[15–17] As is well known, formaldehyde is a kind of toxic and harmful gas which can damage the health of humans and animals. Hence, researchers should pay more attention to the development of an eco-friendly and cost-effective preparation process of carbon aerogels.

Polyimide (PI) is one kind of widely used engineering plastics owing to its excellent mechanical properties, good thermal stability and high glass transition temperature. Since the first polyimide aerogel was prepared by chemical dehydration and high-temperature imidization,[18] polyimide aerogels gained their rapid development,[19–26] and were widely applied in thermal insulators, acoustic insulation, catalysis, dielectric materials, and so on. In order to inherit the excellent properties as well as widen the application fields of polyimide aerogels, carbon aerogels were synthesized by carbonization of polyimide aerogels in this work and were used as electrode materials for supercapacitors.

Owing to their remarkable properties, such as outstanding mechanical elasticity, high specific surface areas (2675 $m^2\ g^{-1}$), large carrier mobility and electrical conductivity,[27–33] two-

State Key Laboratory of Molecular Engineering of Polymers, Department of Macromolecular Science, Fudan University, 220 Handan Road, Shanghai 200433, P. R. China. E-mail: txliu@fudan.edu.cn; Fax: +86-21-65640293; Tel: +86-21-55664197

dimensional (2D) single-layer graphene sheets with sp^2-hybridized conjugated carbon atoms and graphene-based materials have recently emerged as excellent candidates for energy storage, electronics and sensors. And, it has been revealed that the assembly of 2D graphene sheets into 3D graphene network can endow graphene and graphene-based materials with excellent mechanical strengths, fast mass and electron transport kinetics due to the comprehensive performance of graphene and the 3D inter-connected network.[34–39] Li *et al.* prepared highly porous, ultra-low density, compressible yet elastic graphene sheet–nanoribbon hybrid aerogels. These hybrid aerogels had a high specific capacity of 256 F g^{-1} in a three-electrode electrochemical system.[40] Shi *et al.*[41] prepared high performance self-assembled graphene hydrogel (SGH) by a facile one-step hydrothermal method. The electrical conductivity, thermal stability, storage modulus and specific capacitance of SGH are 5×10^{-3} S cm^{-1}, 450–490 kPa and 175 F g^{-1}, respectively. In another work of Shi *et al.*,[42] 3D SGH was fabricated by chemical reduction of GO with sodium ascorbate. The electrical conductivity and the specific capacitance of 3D SGH can reach 1 S cm^{-1} and 240 F g^{-1} at 1.2 A g^{-1}, respectively. Typically, the stability of these 3D graphene assemblies relies on the physical interactions between individual graphene sheets. Therefore, GO sheets can be utilized as an effective crosslinking agent and can easily assemble into 3D interconnected nanostructures.

In this study, we report a simple and eco-friendly fabrication of carbon aerogels by carbonization of graphene crosslinked PI aerogels. GO–poly(amic acid) (PAA) aerogels were first prepared by mixing water-soluble PAA (*i.e.*, polyimide precursor) and GO suspension. Subsequently, the as-prepared GO–PAA aerogels were amidated in nitrogen atmosphere under 100 °C, 200 °C, 300 °C for 1 h, respectively to crosslink PAA with GO and meanwhile GO was reduced to graphene. Finally, graphene/carbon aerogels were obtained by carbonization of graphene crosslinked PI aerogels. Due to the effective crosslinking of graphene, the carbon aerogels had a high specific surface area of 998.7 m^2 g^{-1} and high specific capacitance up to 178.1 F g^{-1} at a current density of 1 A g^{-1}. It suggests that the graphene/carbon aerogels based electrode materials may have potential applications in high performance energy storage devices. To the best of our knowledge, this is the first report on the preparation of carbon aerogels with multi-sized pores by one-step carbonization of graphene/PI aerogels, which is different from the previous approach that involves toxic formaldehyde.

Experimental

Materials

4,4′-oxidianiline (ODA), *N*,*N*-dimethylacetamide (DMAc), pyromellitic dianhydride (PMDA), triethylamine (TEA, 99%), 98% H_2SO_4, 30% H_2O_2, $KMnO_4$, and 37% HCl were commercially purchased from Sinopharm Chemical Reagent Co., Ltd. All chemicals were used without further purification. Natural graphite powder (325 mesh) was purchased from Alfa-Aesar (Ward Hill, MA) and used without further purification. Deionized (DI) water was used as the solvent throughout the experiments. All other reagents were purchased from Aladdin Chemical Reagent, Co., Ltd. and used as received.

Preparation of water-soluble polyimide precursor PAA

Water-soluble PAA oligomer,[43] the precursor of polyimide was synthesized from a polycondensation procedure (Scheme 1) in DMAc using an equivalent molar ratio of 4,4′-ODA and PMDA at 0 °C. The procedure is as follows: 4,4′-ODA (4.31 g) and DMAc (51 g) were added into a 250 mL three-neck round bottom flask fitted with a mechanical stirrer. Once 4,4′-ODA was dissolved completely, 4.69 g PMDA was added, and the mixture was stirred for 5 h at 0 °C. Subsequently, 2.18 g TEA was slowly dropped into the mixture and stirred for another 5 h. Then, a yellow viscous solution of TEA-capped poly(amic acid) (TEA–PAA) with a solid content of 15 wt% was obtained. Finally, the resultant solution was poured into deionized water at 0 °C and deposited. After washing for three times, the TEA–PAA was frozen in refrigerator and freeze-dried for further use.

Preparation of GO suspension and graphene/carbon aerogels

Graphite oxide was prepared from natural graphite according to Hummer's method.[44] The exfoliated GO suspension (8 mg mL^{-1}) was prepared by ultrasonicating the graphite oxide in deionized water for 2 h.

The graphene/carbon aerogels (derived from graphene crosslinked PI aerogels, named as GC-*X*) were prepared *via* a sol–gel process followed by carbonization. Briefly, the TEA–PAA and a certain amount of TEA were first dissolved in deionized water and a quantity of GO suspension was added. The solution was continually stirred for 20 min and then cast into a 20 mL syringe mold (2 cm in diameter), prepared by cutting off the needle end of the syringe and extending the plunger all the way out. It was kept for gelation at room temperature for at least 2 h to form a series of GO–PAA hydrogels. The weight ratio of GO and TEA–PAA in gel was 2 : 100, 4 : 100, 6 : 100 and 10 : 100 and thus the resulted hydrogels were labelled as GO–PAA-2, GO–PAA-4, GO–PAA-6 and GO–PAA-10. Subsequently, the

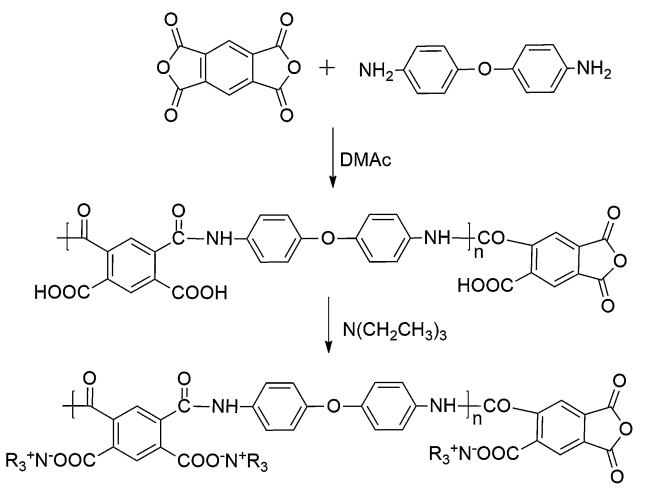

Scheme 1 Reaction scheme of water-soluble polyimide precursor.

hydrogels were frozen and dried in a freeze-dryer. After 24 h in the lyophilizer, the dried samples were heated under vacuum at 100, 200 and 300 °C for 1 h, respectively for complete imidization. After that, a series of graphene crosslinked PI aerogels were obtained, labelled as G–PI-2, G–PI-4, G–PI-6 and G–PI-10, respectively. Finally, the G–PI-*X* aerogels were heated up to 950 °C at a heating rate of 5 °C min^{-1} under N_2 atmosphere, and after 3 h of carbonization the products were cooled naturally. The obtained graphene/carbon aerogels were labelled as GC-2, GC-4, GC-6, and GC-10, respectively. Pure carbon aerogels (derived from pure polyimide aerogel, labelled as GC-0) were also prepared by the same procedure without the addition of GO. Reduced graphene oxide (rGO) was obtained by thermal reduction of graphene oxide under vacuum at 100, 200 and 300 °C for 1 h, respectively.

Characterization

Fourier transform infrared spectra (FT-IR) were measured on a Nicolet 6700 FT-IR spectrometer for G–PI aerogels and typical carbon aerogels (GC-10). Raman spectra were measured on a LabRam-1B French Dilor Com Instruments using a He–Ne laser (λ_{ex} = 632.8 nm). The microstructures were characterized by field-emission scanning electron microscopy (FESEM) (Ultra 55, Zeiss). The specific surface area, pore size distribution, and pore volume were characterized with a belsorp-max surface area detecting instrument (Tristar3000) by N_2 physisorption at 77 K. The pore size distributions were derived from the adsorption branches of isotherms using the Barrett–Joyner–Halenda (BJH) model.

Electrochemical measurements

Prior to all electrochemical measurements, electrodes were prepared according to the method described in previous study.[9] The electrochemical tests were carried out in 6 M KOH aqueous electrolyte solution at room temperature using a typical three electrode cells (Pt wire as counter electrode and Ag/AgCl as reference electrode). Simply, the working electrode was prepared by mixing the powder of graphene/carbon aerogels (before mixing, carbon aerogels were ball-milled at 500 rpm for 2 h), polytetrafluoroethylene (PTFE) and carbon black with a weight ratio of 80 : 10 : 10 and wetted by ethanol to produce homogeneous slurry. The resulting slurry was coated onto the nickel-foam and dried at 80 °C for 12 h, and further pressed under 10 MPa for 60 s. Cyclic voltammetry (CV), galvanostatic charge–discharge curves and electrochemical impedance spectroscopy (EIS) measurements were all performed with a CHI 660D electrochemical workstation (Chenhua Instruments Co, Shanghai, China) at room temperature. CV curves and galvanostatic charge–discharge curves were collected in a voltage ranging from −1 to 0 V. EIS was recorded in the frequency range from 0.01 Hz to 100 kHz at an open circuit potential with amplitude of 5 mV. The specific capacitance of all supercapacitor cells were calculated from the discharge process according to the following equation:

$$C = \frac{I\,\Delta t}{\Delta V \times m}$$

where C is the specific capacitance, I is the current loaded (A), Δt is the discharge time (s), ΔV is the potential change during discharge process (V), and m is the mass of active material in a single electrode (g).

Results and discussion

Graphene/carbon aerogels with hierarchical pores were facilely prepared through a one-step carbonization of graphene crosslinked PI aerogels (Scheme 2). Briefly, PAA solution and GO solution were first mixed together and then the sol–gel process continuously occurred. After freeze-drying, the GO–PAA aerogels with many large macro-pores (200 nm to 2 μm) were obtained due to the sublimation of water. Then the GO–PAA aerogels were imidized completely and GO was crosslinked with PAA during the heating process at 100, 200 and 300 °C for 1 h, respectively. At the same time, GO was reduced to graphene during this thermal treatment. Finally, G–PI aerogels were carbonized into carbon aerogels and during this process, micro- and meso-pores were formed.

Morphology and structure of graphene/carbon aerogels

Fig. 1 presents the FT-IR spectra of GO, PAA, GO–PAA-10, PI, G–PI-10 and GC-10 samples. As seen in Fig. 1, GO shows three prominent characteristic vibrations at 3430, 1735 and 1625 cm^{-1}, corresponding to the broad and intense O–H stretching vibrations, C=O stretching vibrations in carboxylic acid and carbonyl moieties, and C=C stretching vibrations from skeletal vibrations of un-oxidized graphitic domains, respectively. Furthermore, there are two small peaks at 1390 and 1044 cm^{-1},

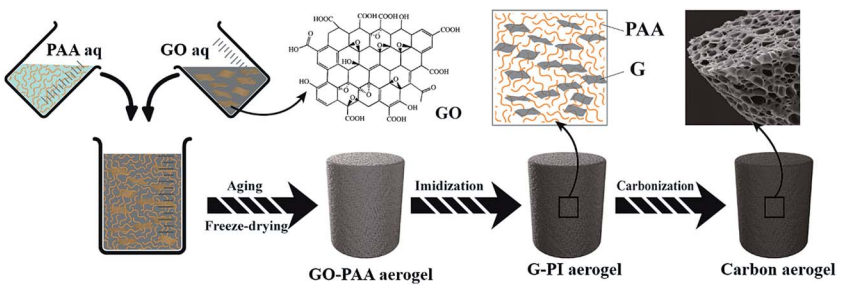

Scheme 2 Schematic illustration of the preparation of graphene/carbon aerogels.

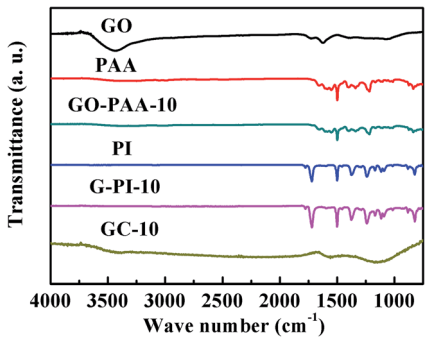

Fig. 1 FT-IR spectra of GO, PAA, GO–PAA-10, PI, G–PI-10, and GC-10 samples.

corresponding to O–H deformation vibrations and C–O stretching vibrations, respectively. These peaks indicate the presence of hydroxyl, carboxylic acid, epoxy groups and other oxygen-containing groups on the surface of the GO sheets. These oxygen-rich functional groups are beneficial for the strong interaction between GO sheets and PAA. For PAA and GO–PAA-10, the characteristic absorption peeks at 1660 cm^{-1} and 1535 cm^{-1} are assigned to the stretching vibrations of C=O and C–N in PAA. However, for the aerogels after imidization, the FT-IR spectrum is dominated by the imide C=O symmetric and asymmetric stretching at 1720 cm^{-1} and 1775 cm^{-1}, respectively, and by the C–N stretching at 1380 cm^{-1}. The absorption at 1510 cm^{-1} is assigned to the C=C stretching, while the peek at 1174 cm^{-1} is attributed to the =C–H in aromatic rings. Therefore, FT-IR measurements prove the successful amidation of PAA to PI and the peak shift of C=O and C–N functional groups probably due to the crosslinking between PAA and GO. However, after calcination, the GC-10 sample only shows an obvious peak at 1625 cm^{-1} and a broad peak at 1100–1200 cm^{-1}, which are ascribed to C=C and C–N stretching vibrations, respectively. Compared to G–PI-10 sample, the absence of the peaks for GC-10 suggests the successful carbonization and removal of oxygen-containing functional groups.

Fig. 2 shows the Raman spectra of GO and rGO samples. As for carbon materials, there are two peaks in the Raman spectrum, corresponding to the D and G bands. The D band is assigned to the conversion of a sp^2-hybridized carbon to a sp^3-hybridized carbon and the G band is related to the vibration of sp^2-hybridized carbon.[45–47] For GO powder, the D band is at 1340 cm^{-1} and the G band is at 1580 cm^{-1}. The Raman spectrum of rGO also shows both D and G bands, but the intensity ratio of D/G increases obviously compared with that of GO, indicating a decrease in the size of the in-plane sp^2 domains and increase of ordered structure formed by thermal reduction.[48]

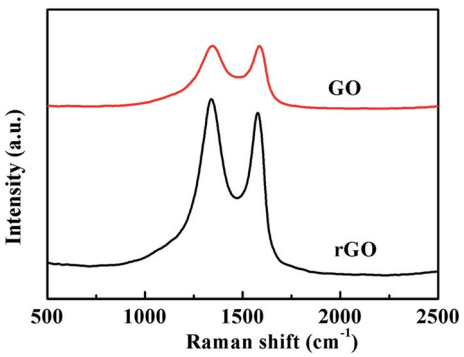

Fig. 2 Raman spectra of GO and rGO samples.

Fig. 3 shows the typical SEM images of the as-synthesized graphene/carbon aerogels with different graphene contents (A–E) and the digital photograph of a graphene/carbon aerogel on a flower (F). Due to the effect of ice-crystal growth and carbonization under N_2 atmosphere, all of these aerogels exhibit highly porous structures with different pore sizes, ranging from several tens of nanometers to several micrometers. Meanwhile, with increasing graphene content, the amount of pores, especially the smaller ones increase. As shown in Fig. 3A, aerogels derived from pure PI aerogels have many large pores (ranging from 1–5 μm) and the wall between the pores was thick. This is probably due to the sublimation of small ice crystals thus leaving pores.[43] From Fig. 3B–E, with addition of graphene, the size of the pores inside carbon aerogels varied from 50 nm to 2 μm. Furthermore, it is obvious that the number of the pores with size from 50 nm to 200 nm is more than those from 1 μm to 2 μm. This may be due to the strong interaction between PAA and GO since there are a lot of carboxyl groups, carbonyls groups and hydroxyl groups on the surface of GO sheets. During the amidation procedure, GO was crosslinked with PAA and the GO–PAA aerogels were imidized completely. Subsequently, by carbonization of G–PI aerogels into graphene/carbon aerogels, micro- and meso-pores were formed. Fig. 3F is the digital photograph of a carbon aerogel on a flower, showing

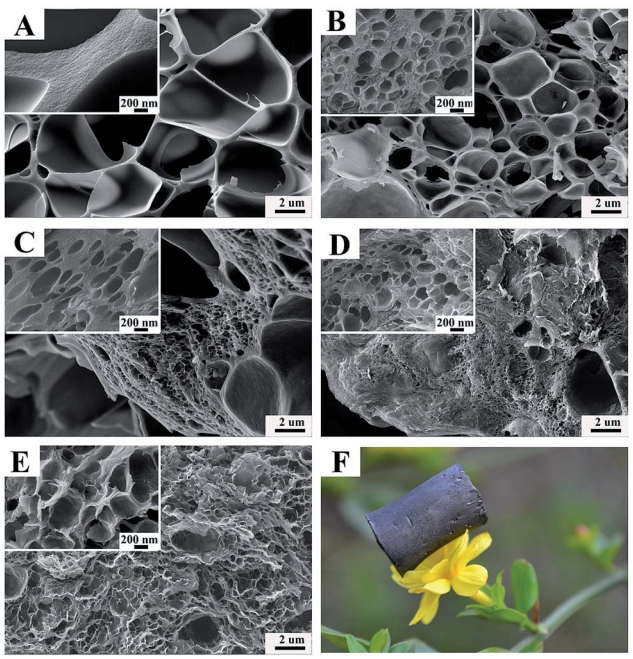

Fig. 3 FE-SEM images of graphene/carbon aerogels (A) GC-0, (B) GC-2, (C) GC-4, (D) GC-6, (E) GC-10 and (F) the digital photograph of a carbon aerogel on a flower.

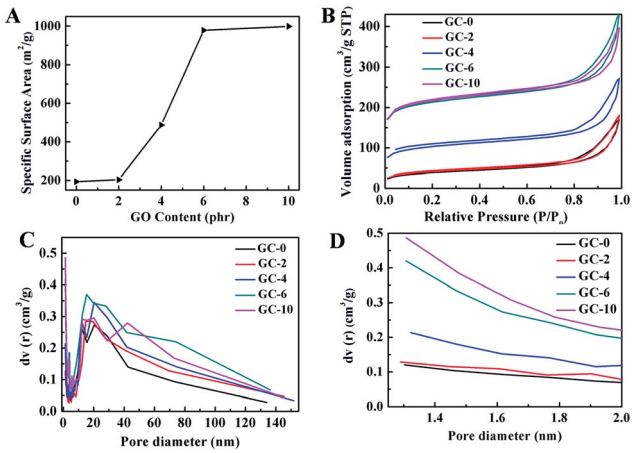

Fig. 4 Porosity of graphene/carbon aerogels by N_2 adsorption–desorption analysis. (A) The specific surface area of graphene/carbon aerogels with different content of graphene. (B) N_2 adsorption–desorption isotherm at 77 K. (C) Pore size distribution as determined by the Barrett–Joynes–Halenda (BJH) method. (D) The enlarged drawing of the pore size ranged from 0–2 nm shows the presence of a range of pores extending from micro to macro scale.

that the density of the prepared carbon aerogels is quite low owing to the multi-porous structures inside themselves, as testified by BET analysis.

Differences of the prepared graphene/carbon aerogels in pore structure and specific surface area are also evidenced in the surface area measurements by nitrogen physisorption, which are shown in Fig. 4. The addition of GO can significantly affect the specific surface area and porous nanostructures of the graphene/carbon aerogels. The specific surface areas of GC-0, GC-2, GC-4, GC-6 and GC-10 are 193.8, 203.7, 487.0, 978.2 and 998.7 $m^2\ g^{-1}$, respectively. It is obvious that the specific surface area of graphene/carbon aerogels becomes larger with the increase of crosslinking agent GO (Fig. 4A). When the amount of GO is too low, most PAA is unable to be crosslinked with GO during the process of imidization. With the increase of GO content, more and more PAA is crosslinked with GO during imidization, thus more small size pores inside graphene/carbon aerogels appear and the wall between the pores becomes thinner. Spontaneously, the specific surface area of graphene/carbon aerogels increases greatly. However, if all functional groups of PAA are reacted with GO, the amount of pores will not further increase, resulting in a saturated specific surface area. Furthermore, as shown in Fig. 4B, all isotherm curves of the graphene/carbon aerogels belong to type IV with a clear hysteresis loop, indicating that all the graphene/carbon aerogels possess large quantity of mesopores. Moreover, the pore size distribution calculated by the BJH method was in the range of 0 to 140 nm, as illustrated in Fig. 4C. Fig. 4D shows an enlarged drawing of the pore size distribution ranging from 1–2 nm. It can be seen that the pore size distribution of GC-0, GC-2 and GC-4 presents a broader distribution centered at 20 nm while GC-6 and GC-10 show a relatively narrow distribution centered at 1.4 nm and a broader distribution ranged from 13 nm to 40 nm. The results are in agreement with the SEM observation. Thus, the pore size of the carbon aerogels can be controlled by changing the amount of graphene.

Electrochemical performance of graphene/carbon aerogels

In order to evaluate the electrochemical performance of the graphene/carbon aerogels derived from G–PI aerogels, CV and galvanostatic charge–discharge measurements were carried out with a three-electrode system in 6.0 M KOH. Fig. 5A shows CV curves of GC-0, GC-2, GC-4, GC-6 and GC-10 samples at a scan rate of 10 mV s^{-1} in the potential range from −1 to 0 V. The curves of all electrodes present a rectangular-like shape without an oblique angle, owing to the effect of electrical double layer (EDL) capacitance. These results indicate that these carbon aerogels have a highly capacitive nature and a small equivalent series resistance (ESR) under rapid charging–discharging process. Furthermore, the area under the CV curves within the potential window can represent the relative specific capacitance of the active electrode materials.[49] Comparing the curves in Fig. 5A, the areas under the CV curves of GC-6 and GC-10 are approximately equal and both of them are larger than those of the other three samples, suggesting that the specific capacitances of GC-6 and GC-10 are the highest among the five samples. The superior electrochemical performance of GC-6 and GC-10 can be attributed to the improved conductivity derived from graphene and rational hierarchical porous nanostructures which would increase the transport paths for both charge and electrolyte ions in the electrode.

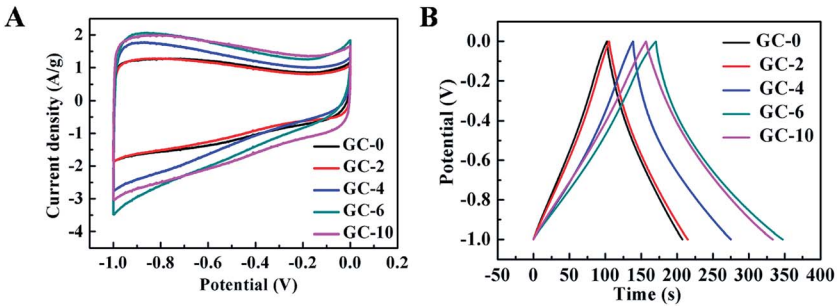

Fig. 5 Electrochemical performance of graphene/carbon aerogel electrode with a three-electrode system in 6.0 M KOH. (A) CV curves at 10 mV s^{-1}. (B) Galvanostatic charge–discharge curves at current density of 1 A g^{-1}.

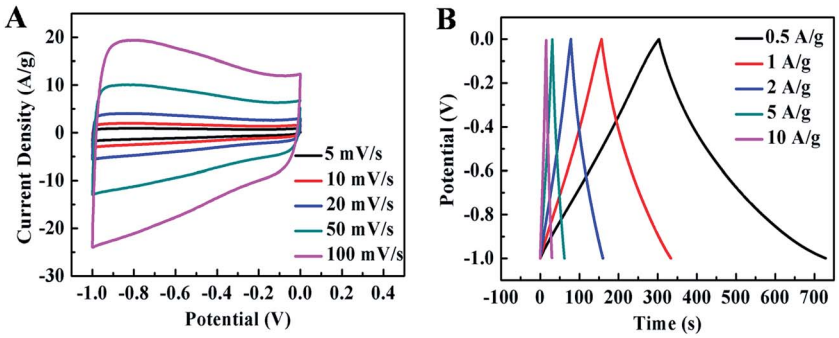

Fig. 6 Electrochemical performance of GC-10 electrode with a three-electrode system in 6.0 M KOH. (A) CV curves at different scan rates. (B) Galvanostatic charge–discharge curve at different current densities.

Fig. 5B is the representative charge–discharge curves of graphene–carbon aerogels at a current density of 1 A g^{-1}. The specific capacitances of GC-0, GC-2, GC-4, GC-6 and GC-10 samples calculated from the discharge process were 104.2, 110.0, 136.5, 176.9 and 178.1 F g^{-1}, respectively. The capacitance of GC-10 is obviously much higher than that of pure carbon aerogels which can only reach an EDL capacitance of less than 105 F g^{-1}. This is probably due to that, with addition of graphene, there are many different sizes of pores inside the graphene/carbon aerogels. Therefore, these hierarchical pores maximize the exposure of their surfaces to electrolyte and provide more different channels for facilitating the transportation of electrolyte ions.

The electrochemical response of GC-10 was performed by CV at various scan rates of 5–100 mV s^{-1}. As shown in Fig. 6A, the shape of the CV curves can approximately be a rectangular mirror image for both the charge and discharge portions when the voltage sweep rate varies from 5 to 100 mV s^{-1}, indicating that GC-10 exhibits excellent electrochemical behavior in a wide range of scan rates. In addition, the obvious increase of peak current density with the scan rates indicates good rate ability for the GC-10 electrode. Fig. 6B shows galvanostatic charge–discharge curves of GC-10 electrode at different current densities. The specific capacitance remained 69% as the current density increased from 0.5 to 10 A g^{-1}, which is mainly due to that the high conductivity of graphene network formed inside carbon aerogels accelerates its charge transfer during the discharging process. Therefore, the graphene/carbon hybrid aerogels can be advantageous in those applications that require high operation voltages owing to their better electrochemical stability across a large voltage range.

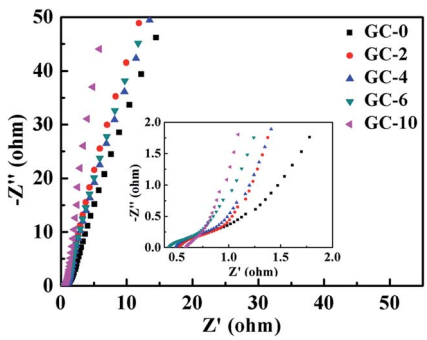

Fig. 7 Nyquist plots for carbon aerogels. Z′, real impedance; Z″, imaginary impedance. The inset shows an enlarged scale.

In order to demonstrate the excellent ion diffusivity and conductivity of these graphene/carbon aerogels, Nyquist impedance spectrum was performed from 0.01 to 100 000 Hz at open-circuit potential. The Nyquist plots of GC-0, GC-2, GC-4, GC-6 and GC-10 hybrid electrodes are shown in Fig. 7. The Nyquist plots of all the carbon aerogel electrodes show an inconspicuous arc in the high frequency region and a straight line in the low-frequency region. The high frequency arc is related to the electronic resistance inside carbon aerogels, and the inconspicuous arc is probably due to the low Faradaic charge transfer resistances.[50] At low frequency, the more vertical the line is, the more closely the supercapacitor behaves as an ideal capacitor due to the fast ion diffusion in the electrode structure.[51] It is obvious that GC-10 sample has the most vertical curve whereas GC-0 sample has the least vertical curve. The solution resistance (R_s) can be obtained from the inter section of the curves at the real axis in the range of high frequency.[49] The values of R_s are about 0.52, 0.5, 0.48, 0.52 and 0.58 Ω corresponding to GC-0, GC-2, GC-4, GC-6 and GC-10 sample, respectively. The low values of R_s for all the graphene/carbon aerogel electrodes may be attributed to the 3D hierarchical network and π–π stacking between graphene and carbon derived from PI, which can facilitate the efficient access of electrolyte ions to the electrode surface and shorten the ion diffusion path.

Conclusions

In summary, novel graphene/carbon aerogels with multimodal pores from micropore to mesopores and macropores were facilely fabricated by one-step carbonization of graphene crosslinked PI aerogels. The corporation of graphene sheets into carbon aerogels can reduce the pore size while increase the amount of micro- and meso-pores as well as increase the electromobility by forming 3D conductive network. The obtained carbon aerogels possess excellent hierarchical porous structure and high specific surface area, which benefits the kinetics for

both charge transfer and ion transport throughout the electrodes. The graphene/carbon aerogels exhibit a maximum specific capacitance of 178.1 F g^{-1} in 6 M KOH electrolyte at current density of 1 A g^{-1}, which is much higher than that of pure carbon aerogels. This work opens a new avenue for obtaining carbon aerogels by an eco-friendly method and also broadens the potential applications of polyimide.

Acknowledgements

The authors are grateful for the financial support from the National Natural Science Foundation of China (51125011, 51433001).

Notes and references

1 C. Moreno-Castilla and F. J. Maldonado-Hódar, *Carbon*, 2005, **43**, 455–465.
2 Y. Q. Li, T. Ben, B. Y. Zhang, Y. Fu and S. L. Qiu, *Sci. Rep.*, 2013, **3**, 2420.
3 X. Shao, W. C. Lu, R. Zhang and F. Pan, *Sci. Rep.*, 2013, **3**, 3018.
4 Y. Yang, Z. Tong, T. Ngai and C. Y. Wang, *ACS Appl. Mater. Interfaces*, 2014, **6**, 6351–6360.
5 Y. Q. Li, Y. A. Samad, K. Polychronopoulou, S. M. Alhassan and K. Liao, *ACS Sustainable Chem. Eng.*, 2014, **2**, 1492–1497.
6 W. Gao, Y. E. Miao, C. Zhang, Z. Yang, Z. Y. Liu, W. W. Tjiu and T. X. Liu, *ACS Appl. Mater. Interfaces*, 2013, **5**, 7584–7591.
7 M. Antonietti, N. Fechler and T. P. Fellinger, *Chem. Mater.*, 2013, **26**, 196–210.
8 W. Xia, B. Qiu, D. G. Xia and R. Q. Zou, *Sci. Rep.*, 2013, **3**, 1935.
9 N. P. Liu, J. Shen and D. Liu, *Microporous Mesoporous Mater.*, 2013, **167**, 176–181.
10 S. Kubo, R. J. White, K. Tauer and M. M. Titirici, *Chem. Mater.*, 2013, **25**, 4781–4790.
11 X. Y. Wang, X. Y. Wang, L. Yi, L. Liu, Y. Z. Dai and H. Wu, *J. Power Sources*, 2013, **224**, 317–323.
12 X. L. Wu and A. W. Xu, *J. Mater. Chem. A*, 2014, **2**, 4852–4864.
13 L. Liu, J. Yang and Q. H. Meng, *J. Sol–Gel Sci. Technol.*, 2013, **67**, 304–311.
14 Z. B. Zulamita, C. M. Francisco and M. Carlos, *Mater. Chem. Phys.*, 2013, **138**, 870–876.
15 Y. Chen and Y. Liu, *J. Mater. Chem. A*, 2014, **2**, 9193–9199.
16 Y. Zhou, S. L. Candelaria, Q. Liu, Y. Huang, E. Uchaker and G. CaO, *J. Mater. Chem. A*, 2014, **2**, 8472–8482.
17 H. Jin, H. Zhang, H. Zhong and J. Zhang, *Energy Environ. Sci.*, 2011, **4**, 3389–3394.
18 C. E. Sroog, *Prog. Polym. Sci.*, 1991, **16**, 561–694.
19 L. Nicholas, S. L. Chariklia, D. P. Mohite, Z. J. Larimore, J. T. Mang, G. Churu and H. B. Lu, *Chem. Mater.*, 2011, **23**, 2250–2261.
20 M. A. B. Meador, E. J. Malow, R. Silva, S. Wright, D. Quade, S. L. Vivod, H. Q. J. Guo and M. Cakmak, *ACS Appl. Mater. Interfaces*, 2012, **4**, 536–544.
21 C. Chakkaravarthy, L. Zachary, S. L. Chariklia, J. T. Mang and L. Nicholas, *J. Mater. Chem.*, 2010, **20**, 9666–9678.
22 J. P. Randall, M. A. B. Meador and S. C. Jana, *ACS Appl. Mater. Interfaces*, 2011, **3**, 613–626.
23 H. Q. Guo, M. A. B. Meador, L. McCorkle, D. J. Quade, J. Guo, B. Hamilton and M. Cakmak, *ACS Appl. Mater. Interfaces*, 2012, **4**, 5422–5429.
24 M. A. B. Meador, E. McMillon, A. Sandberg, E. Barrios, N. G. Wilmoth, C. H. Mueller and F. A. Miranda, *ACS Appl. Mater. Interfaces*, 2014, **6**, 6062–6068.
25 H. Guo, M. A. B. Meador, L. McCorkle, D. J. Quade, J. Guo, B. Hamilton, M. Cakmak and G. Sprowl, *ACS Appl. Mater. Interfaces*, 2011, **3**, 546–552.
26 J. C. Williams, M. A. B. Meador, L. McCorkle, C. Mueller and N. Wilmoth, *Chem. Mater.*, 2014, **26**, 4163–4171.
27 C. G. Lee, X. D. Wei, J. W. Kysar and J. Hone, *Science*, 2008, **321**, 385–388.
28 A. K. Geim and K. S. Novoselov, *Nat. Mater.*, 2007, **6**, 183–191.
29 J. L. Xia, F. Chen, J. H. Li and N. J. Tao, *Nat. Nanotechnol.*, 2009, **4**, 505–509.
30 Y. W. Zhu, S. Murali, M. D. Stoller, K. J. Ganesh, W. W. Cai, P. J. Ferreira, A. Pirkle, R. M. Wallace, K. A. Cychosz, M. Thommes, D. Su, E. A. Stach and R. S. Ruoff, *Science*, 2011, **332**, 1537–1541.
31 M. Pumera, *Energy Environ. Sci.*, 2011, **4**, 668–674.
32 F. Schwierz, *Nat. Nanotechnol.*, 2010, **5**, 487–496.
33 F. Schedin, A. K. Geim, S. V. Morozov, E. W. Hill, P. Blake, M. I. Katsnelson and K. S. Novoselov, *Nat. Mater.*, 2007, **6**, 652–655.
34 W. F. Chen, S. Li, C. H. Chen and L. F. Yan, *Adv. Mater.*, 2011, **23**, 5679–5683.
35 Z. S. Wu, Y. Sun, Y. Z. Tan, S. B. Yang, X. L. Feng and K. Müllen, *J. Am. Chem. Soc.*, 2012, **134**, 19532–19535.
36 M. A. Worsley, S. O. Kucheyev, H. E. Mason, M. D. Merrill, B. P. Mayer, J. Lewicki, C. A. Valdez, M. E. Suss, M. Stadermann, P. J. Pauzauskie, J. H. Satcher, J. Biener and T. F. Baumann, *Chem. Commun.*, 2012, **48**, 8428–8430.
37 H. Hu, Z. B. Zhao, W. B. Wan, Y. Gogotsi and J. S. Qiu, *Adv. Mater.*, 2013, **25**, 2219–2223.
38 M. Chen, C. Zhang, X. Li, L. Zhang, Y. Ma, L. Zhang, X. Xu, F. Xia, W. Wang and J. Gao, *J. Mater. Chem. A*, 2013, **1**, 2869–2877.
39 J. Li, J. Li, H. Meng, S. Xie, B. Zhang, L. Li, H. Ma, J. Zhang and M. Yu, *J. Mater. Chem. A*, 2014, **2**, 2934–2941.
40 C. H. Wang, X. D. He, Y. Y. Shang, Q. Y. Peng, Y. Y. Qin, E. Z. Shi, Y. B. Yang, S. T. Wu, W. J. Xu, S. Y. Du, A. Y. Cao and Y. B. Li, *J. Mater. Chem. A*, 2014, **2**, 14994–15000.
41 Y. X. Xu, K. X. Sheng, C. Li and G. Q. Shi, *ACS Nano*, 2010, **4**, 4324–4330.
42 K. X. Sheng, Y. X. Xu, C. Li and G. Q. Shi, *New Carbon Mater.*, 2011, **26**, 9–15.
43 W. Wu, K. Wang and M. S. Zhan, *Ind. Eng. Chem. Res.*, 2012, **51**, 12821–12826.
44 W. S. Hummers and R. E. Offeman, *J. Am. Chem. Soc.*, 1958, **80**, 1339.
45 H. L. Guo, X. F. Wang, Q. Y. Qian, F. B. Wang and X. H. Xia, *ACS Nano*, 2009, **3**, 2653–2659.
46 W. Fan, Y. Y. Xia, W. W. Tjiu, P. K. Pallathadka, C. B. He and T. X. Liu, *J. Power Sources*, 2013, **243**, 973–981.

47 C. Z. Zhu, S. J. Guo, Y. X. Fang and S. J. Dong, *ACS Nano*, 2010, **4**, 2429–2437.
48 S. Stankovich, D. A. Dikin, R. D. Piner, K. A. Kohlhaas, A. Kleinhammes, Y. Y. Jia, Y. Wu, S. T. Nguyen and R. S. Ruoff, *Carbon*, 2007, **45**, 1558–1565.
49 J. Li, H. Q. Xie, Y. Li, J. Liu and Z. X. Li, *J. Power Sources*, 2011, **196**, 10775–10781.
50 Y. Wang, Z. Q. Shi, Y. Huang, Y. F. Ma, C. Y. Wang, M. M. Chen and Y. S. Chen, *J. Phys. Chem. C*, 2009, **113**, 13103–13107.
51 H. L. Wang, Q. L. Hao, X. J. Yang, L. D. Lu and X. Wang, *ACS Appl. Mater. Interfaces*, 2010, **2**, 821–828.